

Suzaku Observation of the *Fermi* Cygnus Cocoon: Search for a Signature of Young Cosmic-Ray Electrons

T. Mizuno¹, T. Tanabe¹, H. Takahashi¹, K. Hayashi², R. Yamazaki³, I. Grenier⁴, L. Tibaldo⁵,

mizuno@hep01.hepl.hiroshima-u.ac.jp

ABSTRACT

The origin of Galactic cosmic rays remains unconfirmed, but promising candidates for their sources are found in star-forming regions. We report a series of X-ray observations, with *Suzaku*, toward the nearby star-forming region of Cygnus X. They aim at comparing diffuse X-ray emissions on and off the γ -ray cocoon of hard cosmic rays revealed by *Fermi* LAT. After excluding point sources and small-scale structures and subtracting the non-X-ray and cosmic X-ray backgrounds, the 2–10 keV X-ray intensity distribution is found to monotonically decrease with increasing Galactic latitude. This indicates that most of the extended emission detected by *Suzaku* originates from the Galactic ridge. In two observations, we derive upper limits of 3.4×10^{-8} erg s⁻¹ cm⁻² sr⁻¹ and 1.3×10^{-8} erg s⁻¹ cm⁻² sr⁻¹ to X-ray emission in the 2–10 keV range from the γ -ray cocoon. These limits exclude the presence of cosmic-ray electrons with energies above about 50 TeV at a flux level capable of explaining the γ -ray spectrum. They are consistent with the emission cut-off observed near a TeV in γ rays. The properties of Galactic-ridge and local diffuse X-rays are also discussed.

Subject headings: ISM: cosmic-rays — X-rays: diffuse background — X-rays: ISM — gamma rays: general

1. Introduction

An important question of modern astrophysics is the origin and propagation of Galactic cosmic rays (GCRs), which are charged particles with relativistic energies (up to 10^{15-16} eV) diffusing in

¹Hiroshima University

¹ISAS/JAXA

¹Aoyama Gakuin University

¹CEA Sacray

¹SLAC National Accelerator Laboratory

and around the Milky Way. At low energy, they directly affect the chemistry and thermodynamics of interstellar matter through ionization, heating, and pressure. Supernova remnants (SNRs) are widely considered as the most plausible sources of GCRs, because they are energetic and numerous enough to maintain the power of GCRs (e.g., Ginzburg & Syrovatskii 1964). Because the massive OB stars (the progenitors of core-collapse supernovae) are born in clusters and live shortly, supernova explosions tend to cluster in space (within a few parsecs) and in time (within a few 10^5 years) (Higdon & Lingenfelter 2005). Therefore, GCRs are expected to be accelerated and injected into the interstellar space, not only by the ensembles of individual SNRs, but also by overlapping shocks from SNRs and massive stellar winds (called superbubbles, Tenorio-Tagle & Bodenheimer 1988) created around OB associations (e.g., Bykov & Fleishman 1992; Parizot et al. 2004). However, this scenario about GCR origin requires observational confirmation.

Recently, the Large Area Telescope (LAT) on the *Fermi* Gamma-Ray Space Telescope (Atwood et al. 2009) has revealed an extended source of hard, multi-GeV γ rays, called the "Cygnus cocoon" (Ackermann et al. 2011), in the nearby star-forming region known as Cygnus X (e.g., Piddington & Minnett 1952; Uyaniker et al. 2001), at a distance of ~ 1.4 kpc (Rygl et al. 2012). The extended emission is detected with high confidence above the interstellar γ -ray background and after subtraction of known point sources, at energies above 1 GeV. The emission morphology corresponds to the region bounded by the ionization fronts powered by the numerous OB stars present in the region. The morphology and the absence of marked spectral variations across the cocoon imply an interstellar origin rather than a superposition of unresolved γ -ray sources. The observed γ -ray spectrum cannot be explained by the GCR proton or electron spectra measured at the Earth and in the local interstellar medium. The latter is often referred to as the Local Interstellar Spectrum (LIS). An amplification factor of $(1.5\text{--}2) \times (E_p/10 \text{ GeV})^{0.3}$ of the LIS proton spectrum, or of $\sim 60 \times (E_e/10 \text{ GeV})^{0.5}$ of the LIS electron spectrum, is required to explain the cocoon emission (where E_p and E_e respectively denote the energy of the CR proton and electron in the cocoon). The intense and hard γ -ray spectrum thus indicates the presence of freshly-accelerated CRs in the cocoon.

Fermi-LAT data alone, however, cannot constrain the dominant type of radiating particles (protons or electrons), nor the maximum energy of the electrons. For this purpose, γ -ray observations are usefully complemented by X-ray observations, which are sensitive to CR electrons at TeV energies. We have therefore conducted deep X-ray observations of the γ -ray cocoon region using the X-ray Imaging Spectrometer, XIS (Koyama et al. 2007) on board *Suzaku* satellite (Mitsuda et al. 2007), which is very sensitive to extended X-ray emission. If the cocoon γ -ray emission is produced by interactions of CR electrons with the interstellar radiation field and the particles accelerated beyond 10 TeV in energy have not yet cooled or escaped the region, we expect to find extended non-thermal X-ray emission due to synchrotron radiation in the large magnetic field of $\sim 20 \mu\text{G}$ inferred in the region (Ackermann et al. 2011).

2. Observations and Data Reduction

To constrain the CR properties in the cocoon, we have performed a series of X-ray observations of the Cygnus region. Two “source” observations were pointed at positions with strong GeV cocoon emission, but free of known, bright X-ray sources, such as the SNR γ Cygni and the binary Cygnus X-3. Because a potential X-ray counterpart to the cocoon is likely to fill the whole field of view of the XIS instrument, we have also conducted two “background” observations to estimate the backgrounds in the Cygnus direction, in particular the intensity of the Galactic ridge X-ray emission (GRXE; Worrall et al. 1982; Warwick et al. 1985; Koyama et al. 1986). The GRXE is an apparently diffuse feature along the Galactic plane and its origin would be a mixture of truly diffuse hot plasma and numerous dim point sources (e.g., Ebisawa et al. 2005; Revnivtsev et al. 2006; Uchiyama et al. 2013). The positions of the four observations are overlaid on the γ -ray count map of the cocoon in Figure 1.

The observations were carried out using the XIS on the focal plane of the X-Ray Telescope (XRT; Serlemitsos et al. 2007) on *Suzaku*. The XIS consists of two front-illuminated (FI) X-ray CCDs (XIS0 and 3)¹ and one backside-illuminated (BI) X-ray CCD (XIS1). The combined XIS and XRT system is sensitive within the energy range 0.3–12 keV. Although its angular resolution is moderate (half-power diameter $\sim 2'$), the XIS+XRT system provides a low and stable instrumental background (Mitsuda et al. 2007; Tawa et al. 2008); therefore it is suitable for the study of extended emission with low surface brightness. The XIS was operated in the normal clocking full-frame mode, and data were recorded in the 3×3 or 5×5 editing mode. Data were analyzed using the HEADAS 6.15.1 software with the calibration database released on July 1, 2014. We reprocessed data using *aepipeline* to take the latest calibration into account. We analyzed the so-called cleaned events, which had passed the following standard event selection criteria: a) only *ASCA*-grade 0, 2, 3, 4, and 6 events were accumulated with hot and flickering pixels removed; b) more than 436 s had elapsed since passing through the South Atlantic Anomaly; and c) the pointing direction was at least 5° and 20° above the rim of the Earth during night and day, respectively. To further reduce the non-X-ray background (NXB), we also required that d) the geomagnetic cutoff rigidity exceeded 6 GV. Details concerning the observation and net exposures of the screened events are summarized in Table 1.

¹Because of an anomaly occurred in 2006 November, the operation of another FI sensor, XIS2, has been terminated.

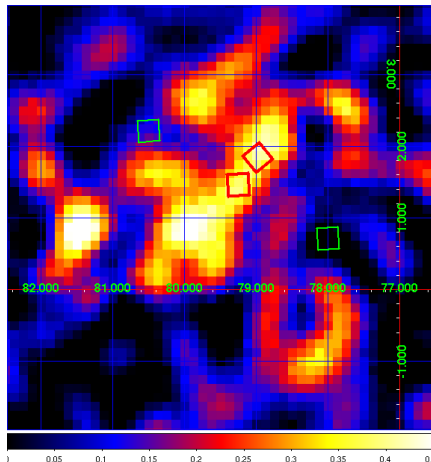


Fig. 1.— Positions of X-ray observations overlaid on the γ -ray residual count map of the cocoon above 10 GeV, smoothed with a $\sigma = 0.^\circ25$ Gaussian kernel (Ackermann et al. 2011). The unit of the γ -ray map is counts per pixel after the smoothing was applied. The coordinates are in Galactic longitude and latitude. Source and background observations are indicated by thick red and thin green boxes, respectively. See Table 1 for details.

Table 1: Summary of observations

Region	Pointing ^a		Observation date	Net exposure (ks)
	l (deg)	b (deg)		
Source 1	79.25	1.49	2012 Nov 18	43.3
Source 2	78.99	1.86	2013 Dec 07	42.0
Background 1	78.00	0.74	2012 Nov 19	19.9
Background 2	80.50	2.24	2012 Nov 19	25.6

^al and b are Galactic longitude and latitude of the center of the XIS field-of-view, respectively.

3. Data Analysis and Results

3.1. X-ray Images

We have extracted X-ray images from the two FI CCDs (XIS0 and XIS3). These cameras have better imaging quality than the BI CCD (XIS1) due to their lower instrumental background. We have defined the soft and hard bands as 0.7–2 keV and 2–10 keV, respectively, and have excluded the corners of the CCD chips illuminated by the ^{55}Fe calibration sources. We have then estimated the NXB contribution from the night Earth data and subtracted it from the images using `xisnxbgen` (Tawa et al. 2008). Vignetting was then corrected by dividing the soft- and hard-band images by flat sky images simulated at 1 keV and 4 keV, respectively, by using the XRT+XIS simulator `xissim` (Ishisaki et al. 2007). In the flat image simulations, we have assumed a uniform intensity of $1 \text{ photon s}^{-1} \text{ cm}^{-2} \text{ sr}^{-1}$, thus the approximate unit of the obtained vignetting-corrected image is $\text{photons s}^{-1} \text{ cm}^{-2} \text{ sr}^{-1}$. We have combined two FI CCD images and applied smoothing with a Gaussian kernel of $\sigma = 0.28$ for visualization. Several point sources and small-scale structures are recognizable in the final images (see Figure 2). Moreover, we also observe strong, apparently extended emission in the soft-band images of Source 2 and Background 2 observations. In the hard-band images, the apparently extended emission is more intense in Source 1 and Background 1 than in the other two regions.

3.2. Extended Emission Spectra

We have extracted extended emission based on the vignetting-corrected images (Figure 2). We have first identified point sources and small-scale structures in each of the soft- and hard-band images by eye and have delineated them by $1.5'$ radius circular regions (green circles in Figure 2). These structures have been designated as `src1`, `src2`, etc. in each field, and events in those circles have been removed². Spectral analysis of these sources and structures is described in § 3.2 and results are summarized in Table 3. An $80 \text{ pixel} \times 1024 \text{ pixel}$ rectangular region and an area with (occasionally) significantly high background at the corner of the chip are unusable in XIS1³. For simplicity, these regions have been excluded from the sky projections for all XIS camera images. We have then accumulated the extended X-ray emission spectra by integrating the events over the whole XIS field of view ($\sim 17.8 \times 17.8$), and analyzed the spectra for diffuse X-ray emission with ancillary response files (ARFs) calculated by `xissimarfgen` (Ishisaki et al. 2007), assuming uniform brightness over a $20'$ radius. The loss of effective area due to the exclusion of point sources and

² Although the choice of sources and structures is not unique, the effect on the estimated extended emission is small. For example, even if we included `src3` (a moderately bright source located close to the center of the field of view) of Source 1 observation, the 2–10 keV intensity of the extended emission was increased by $\sim 0.3 \times 10^{-8} \text{ erg s}^{-1} \text{ cm}^{-2} \text{ sr}^{-1}$ which is less than half of the uncertainty examined in § 4.1 and shown in Figure 5

³ See “The Suzaku Data Reduction Guide” of v5.0 (<http://www.heasarc.gsfc.nasa.gov/docs/suzaku/analysis/abc>)

unusable area described above has been taken into account in calculating the ARFs. The response matrix files (RMFs) has been calculated with `xisrmfgen`, and the NXB spectrum integrated over the same region as that for the extended emission has been estimated by `xisnxbgen` (Tawa et al. 2008) and subtracted from the source spectrum. In our observations, the energy resolution degraded by particle radiation was restored by a spaced-row charge-injection technique (e.g., Uchiyama et al. 2009a) with a 6 keV equivalent charge applied on orbit. The amount of the charge injected affects the NXB level of the XIS, and was taken into account in calculating the NXB.

The NXB-subtracted X-ray spectrum is expected to be a sum of the cosmic X-ray background (CXB), the GRXE (plus local diffuse X-ray emission), and the possible X-rays from the cocoon. Following Kushino et al. (2002), the CXB has been modelled as a fixed power law with a photon index of 1.4 and a normalization of 9.42×10^{-4} photons $\text{s}^{-1} \text{cm}^{-2} \text{keV}^{-1}$ at 1 keV, or a 2–10 keV flux of 6.20×10^{-12} erg $\text{s}^{-1} \text{cm}^{-2}$, corresponding to an intensity of 5.85×10^{-8} erg $\text{s}^{-1} \text{cm}^{-2} \text{sr}^{-1}$ integrated throughout the 20' radius. Adopting the optically-thin approximation, from Kalberla et al. (2005) we have estimated the neutral hydrogen column density toward the regions studied here as $\sim 1.3 \times 10^{22} \text{cm}^{-2}$. However, the opacity of the H I 21 cm line is non-negligible in the Galactic plane (e.g., Ackermann et al. 2012a), and contribution from molecular clouds and dark neutral medium (e.g., Grenier et al. 2005) should be taken into account. We therefore estimated total neutral hydrogen column density from γ -ray data in these regions based on the analysis by Ackermann et al. (2012b). We adopted spin temperature of 250 K as a baseline model and obtained the total column density $N(\text{H})$ of $(2.5\text{--}3.1) \times 10^{22} \text{cm}^{-2}$, giving the 2–10 keV intensity of $(4.8\text{--}5.0) \times 10^{-8}$ erg $\text{s}^{-1} \text{cm}^{-2} \text{sr}^{-1}$ (see Table 2). The uncertainty due to the assumed spin temperature is evaluated in § 4.1. Based on previous studies of the GRXE and local diffuse X-ray emission (e.g., Kaneda et al. 1997; Uchiyama et al. 2009b; Kataoka et al. 2013), we modeled the GRXE (plus local diffuse X-ray emission) as `vapex1+wabs2×apex2+wabs3×apex3` in XSPEC, where `apex` (and `vapex`) and `wabs` are thin-thermal plasma models by Smith et al. (2001) and interstellar absorption by Morrison & McCammon (1983), respectively. We have allowed the relative normalizations among the three XIS sensors to vary. Among three components, the first term (low-temperature plasma model) represents the unabsorbed Local Bubble emission and/or contamination from the Solar-Wind Charge eXchange (SWCX) (e.g., Fujimoto et al. 2007), and we have fixed the plasma temperature and abundance to $kT = 0.1$ keV and $Z = Z_{\odot}$, respectively (see, e.g., Smith et al. 2007; Yoshino et al. 2009). The second and the third terms (mid-temperature and high-temperature plasma models) correspond to the classical soft-temperature and hard-temperature emissions of the GRXE, respectively (e.g., Kaneda et al. 1997). In all four observations, we have found that our low-temperature plasma model is not able to reproduce the data in the energy range of 0.5–0.6 keV, because the observed energy of the emission line is lower than the O VII resonance line energy (0.574 keV). We have therefore set the Oxygen abundance to 0 and added a gaussian line at ~ 0.56 keV with the line center energy and normalization allowed to vary. The line is likely to be due to a charge-exchange process, as described in § 4.2. We have also added lines at ~ 0.65 keV (to reproduce the line of O VIII) and at 6.40 keV (to reproduce Fe K_{α} line) if the presence of the line was significant at the 99% confidence from an F-test. Our CXB+GRXE (plus local diffuse

X-ray emission) model successfully reproduces the Source 1 observation data (reduced chi-square $\chi^2/\text{d.o.f.} = 538.1/501$). As shown in Figure 3, low-, middle- and high-temperature plasma models dominate the spectrum below ~ 0.7 keV, from ~ 0.7 to ~ 2 keV and above ~ 2 keV, respectively. Above 2 keV, the contributions from the CXB (fixed to a model described above) and the high-temperature plasma model are comparable. These two components are degenerate to a large extent in spectral shape, and the effect of the CXB uncertainty on the remaining hard-band intensity is described in § 4.1. The results from the fits in the four regions are summarized in Table 2 and Figure 4.

3.3. Spectra of Individual Point Sources and Small-scale Structures

To study point sources and small-scale structures, we have integrated the events within the $1'.5$ radius circular regions shown in Figure 2. If the $1'.5$ radius was too large and contaminated from nearby sources (e.g., src1 and src2 in Source 1 observation) or if the source was close to the edge of the CCD chip (e.g., src6 in Source 1 observation), the radius has been reduced to $1'$. The RMF and ARF have been calculated by `xismfgen` and `xisarfgen`, respectively, assuming a point-source response in the latter. For the spectral fitting, we have used an absorbed power-law model (`wabs × pow` in XSPEC) or an absorbed thin-thermal plasma model (`wabs × apec` in XSPEC). We have first tried a power-law model and employed a thin-thermal plasma model if the power-law model was inadequate; i.e., if we observed large residuals in the fit or if the best-fit photon index were excessively large ($\Gamma \geq 3$). Src3 in Source 1 observation was not well fitted by a single component model, so we have fitted its spectrum using a two-component model (`apec+pow` with the common absorption). The fits results are summarized in Table 3. The majority of sources have a hard power-law spectrum with a photon index Γ of ≤ 2.5 and relatively large absorption ($N(\text{H}) \geq 2 \times 10^{22} \text{ cm}^{-2}$). These sources (src2, src4 and src5 in Source 1 observation, src1 and src2 in Source 2 observation, src1 in Background 1 observation and src1 in Background 2 observation) are most likely background active-galactic nuclei. According to Tozzi et al. (2001) who compiled the $\log N - \log S$ relation of X-ray sources, the expected number of active-galactic nuclei with 2–10 keV flux $\geq 0.5 \times 10^{-13} \text{ erg s}^{-1} \text{ cm}^{-2}$ is $\sim 30/\text{deg}^2$. This implies 2–3 uncatalogued active-galactic nuclei in each XIS field-of-view, which is close to the number of sources we found. Possible counterparts, identified from the SIMBAD⁴ and NED⁵ databases within $1'$ of the source position, are also listed in Table 3.

⁴<http://simbad.u-strasbg.fr/simbad/sim-fcoo>

⁵<http://ned.ipac.caltech.edu/>

Table 2: Best-fit spectral parameters of extended emission

	Source1	Source2	Background1	Background2
E_1 (keV)	0.548 ± 0.004	0.545 ± 0.006	0.551 ± 0.007	$0.554^{+0.009}_{-0.010}$
Norm ₁	$23.8^{+3.7}_{-3.9}$	24.4 ± 3.1	$22.1^{+5.4}_{-4.7}$	$14.9^{+5.3}_{-4.0}$
E_2 (keV)	0.653(fixed) ^a	$0.648^{+0.013}_{-0.014}$	$0.673^{+0.031}_{-0.035}$	–
Norm ₂	$2.3^{+0.8}_{-0.9}$	5.3 ± 1.1	$2.0^{+0.9}_{-0.8}$	–
E_3 (keV)	6.40(fixed)	–	–	–
Norm ₃	$0.12^{+0.09}_{-0.10}$	–	–	–
$N(\text{H})_{\text{low}}$ (10^{22} cm ⁻²)	0(fixed)	0(fixed)	0(fixed)	0(fixed)
kT_{low} (keV)	0.1(fixed)	0.1(fixed)	0.1(fixed)	0.1(fixed)
A_{low} (Z_{\odot})	1(fixed)	1(fixed)	1(fixed)	1(fixed)
EM_{low}	103 ± 18	144^{+21}_{-20}	99^{+23}_{-24}	139^{+36}_{-34}
$N(\text{H})_{\text{mid}}$ (10^{22} cm ⁻²)	$0.39^{+0.07}_{-0.09}$	$0.46^{+0.04}_{-0.06}$	$0.73^{+0.11}_{-0.14}$	$0(\leq 0.02)$
kT_{mid} (keV)	$0.73^{+0.02}_{-0.03}$	0.62 ± 0.02	$0.62^{+0.11}_{-0.04}$	$0.60^{+0.02}_{-0.01}$
A_{mid} (Z_{\odot})	$0.13^{+0.06}_{-0.04}$	$0.29^{+0.27}_{-0.10}$	$0.27^{+1.25}_{-0.15}$	$0.37^{+1.22}_{-0.11}$
EM_{mid}	256^{+31}_{-49}	242^{+64}_{-98}	$(20^{+9}_{-16}) \times 10$	73^{+26}_{-31}
$N(\text{H})_{\text{high}}$ (10^{22} cm ⁻²)	$3.1^{+1.4}_{-1.5}$	$1.9(\leq 3.0)^{\text{b}}$	$2.6^{+0.8}_{-1.0}$	$2.0^{+0.7}_{-1.4}$
kT_{high} (keV)	$3.1^{+2.4}_{-0.9}$	$2.6^{+1.0}_{-0.6}$	$2.4^{+0.8}_{-0.4}$	$1.5^{+1.7}_{-0.3}$
A_{high} (Z_{\odot})	$0.36^{+0.22}_{-0.17}$	$0.28^{+0.31}_{-0.26}$	$0.19^{+0.16}_{-0.14}$	$0.4(\leq 1.1)$
EM_{high}	106^{+59}_{-43}	76^{+39}_{-23}	217^{+78}_{-65}	103^{+65}_{-37}
I_{low} (0.5–10 keV) ^c	2.46×10^{-8}	2.86×10^{-8}	2.38×10^{-8}	1.55×10^{-8}
I_{mid} (0.5–10 keV) ^c	5.66×10^{-8}	6.38×10^{-8}	3.01×10^{-8}	8.42×10^{-8}
I_{high} (0.5–10 keV) ^c	4.88×10^{-8}	3.15×10^{-8}	7.20×10^{-8}	2.39×10^{-8}
$N(\text{H})_{\text{CXB}}$ (10^{22} cm ⁻²)	2.92(fixed)	2.47(fixed)	3.07(fixed)	2.67(fixed)
I_{CXB} (0.5–2 keV) ^c	0.12×10^{-8} (fixed)	0.16×10^{-8} (fixed)	0.11×10^{-8} (fixed)	0.14×10^{-8} (fixed)
I_{CXB} (2–10 keV) ^c	4.85×10^{-8} (fixed)	4.97×10^{-8} (fixed)	4.81×10^{-8} (fixed)	4.92×10^{-8} (fixed)
$I_{0.5-2}^{\text{c}}$	7.69×10^{-8}	9.22×10^{-8}	5.72×10^{-8}	10.44×10^{-8}
I_{2-10}^{c}	10.29×10^{-8}	8.33×10^{-8}	11.79×10^{-8}	6.98×10^{-8}
$\chi^2/\text{d.o.f.}$	538.1/501	565.7/521	320.1/252	370.5/336

E and Norm are line center energy (keV) and the intensity (photons s⁻¹ cm⁻² sr⁻¹) of gaussian, respectively. $N(\text{H})_{\text{low}}/kT_{\text{low}}/A_{\text{low}}/EM_{\text{low}}$, $N(\text{H})_{\text{mid}}/kT_{\text{mid}}/A_{\text{mid}}/EM_{\text{mid}}$ and $N(\text{H})_{\text{high}}/kT_{\text{high}}/A_{\text{high}}/EM_{\text{high}}$ are absorption/temperature/abundance/emission measure of the low-, middle- and high-temperature plasma models, respectively. The emission measures are given as the value integrated over the line-of-sight, $\frac{1}{4\pi} \int n_e n_H ds$ (where n_e and n_H are the electron and hydrogen density, respectively) in the unit of 10^{14} cm⁻⁵ sr⁻¹. I_{low} , I_{mid} and I_{high} are absorption-uncorrected intensity of low-, middle- and high-temperature components, respectively, where associated line fluxes are also included. $N(\text{H})_{\text{CXB}}$ and I_{CXB} are the assumed column density and absorption-uncorrected intensity of the CXB model, respectively. $I_{0.5-2}$ and I_{2-10} are intensity in 0.5–2 and 2–10 keV including CXB contribution, respectively.

^aThe line center energy was not well determined and thus fixed at the energy of O VIII K_α line.

^bThe Lower limit was set at 1.0×10^{22} cm⁻², otherwise the fit gives unphysical results. ($A_{\text{mid}} \sim 5$, $A_{\text{high}} \sim 0$ and $N(\text{H})_{\text{high}} \sim 0$)

^cThe unit is given in erg s⁻¹ cm⁻² sr⁻¹.

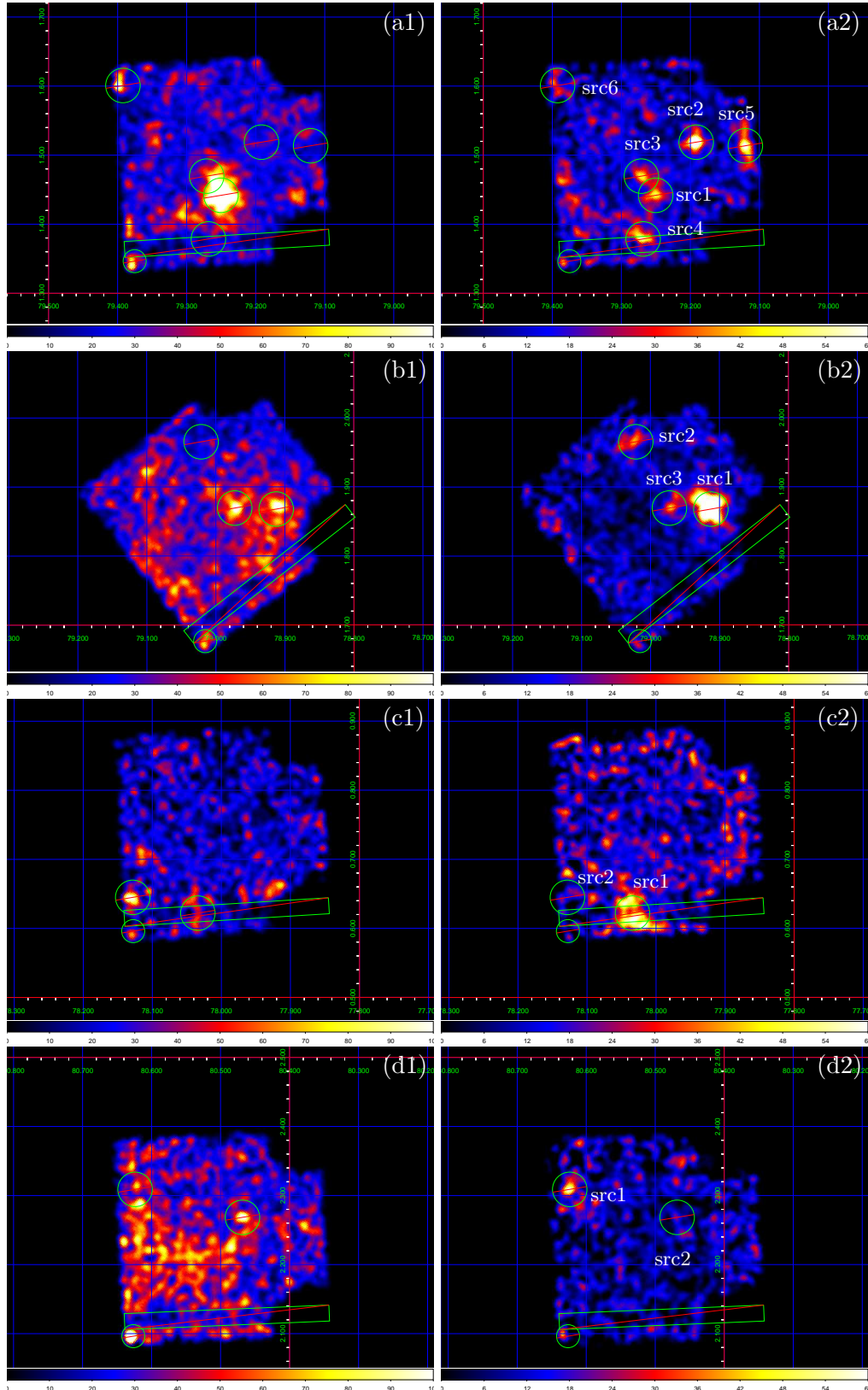


Fig. 2.— From top to bottom: X-ray intensity maps in Galactic coordinates of Source 1 observation (panels a), Source 2 observation (panels b), Background 1 observation (panels c), and Background 2 observation (panels d). Left and right panels show the soft- (0.7–2 keV) and hard-band (2–10 keV) images, respectively.

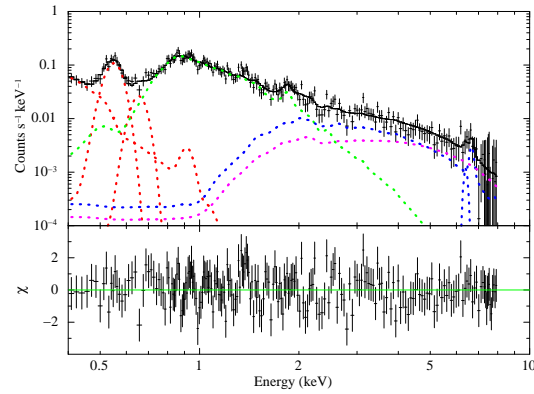


Fig. 3.— Data and modeled spectra of extended X-ray emission of Source 1 region, taken by XIS1. The spectrum is fitted by three-temperature thin-thermal plasmas (GRXE plus local diffuse X-rays) and a fixed power law (CXB). Low-, middle-, and high-temperature models are indicated by red, green, and blue dotted lines, respectively, and the CXB contribution is shown by the dotted purple line. The bottom panel shows the residuals.

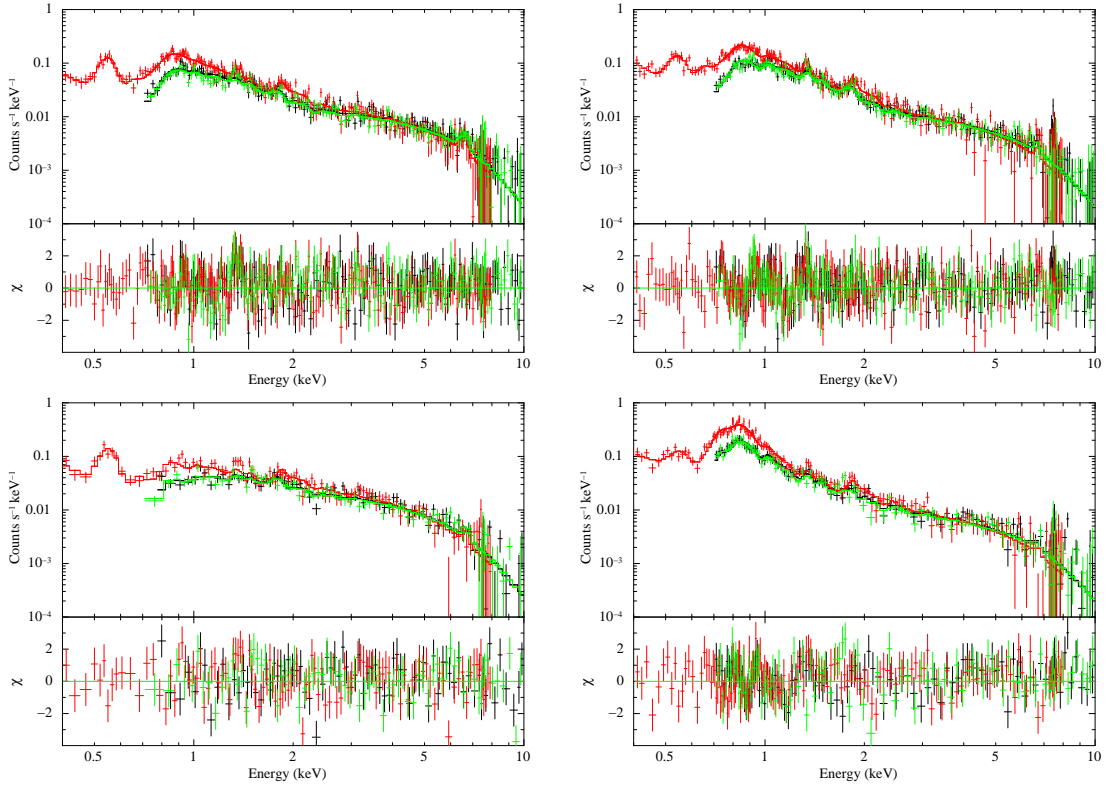


Fig. 4.— X-ray spectra of extended emissions integrated over the XIS field-of-view of Source 1 observation (top left), Source 2 observation (top right), Background 1 observation (bottom left), and Background 2 observation (bottom right). The XIS0, 1, and 3 data are indicated by black, red, and green crosses, respectively. Solid lines are the best-fit models. The bottom panels show the residuals.

Table 3: Spectra of point sources and small-scale structures

Region/source	N_{H} 10^{22} cm^{-2}	Γ	kT keV	A Z_{\odot}	$f_{0.5-2}$ $\text{erg s}^{-1} \text{ cm}^{-2}$	f_{2-10} $\text{erg s}^{-1} \text{ cm}^{-2}$	$\chi^2/\text{d.o.f.}$	possible counterpart ^a
Source 1								
src1	0.03(≤ 0.09)	–	0.94 $^{+0.08}_{-0.14}$	0.07 \pm 0.03	1.81 $\times 10^{-13}$	0.29 $\times 10^{-13}$	71.6/64	1RXS J202725.2+405428
src2	5.1 $^{+5.2}_{-2.7}$	2.3 $^{+1.5}_{-1.0}$	–	–	0.03 $\times 10^{-13}$	1.52 $\times 10^{-13}$	41.6/40	NVSS J202655+405408
src3	0.79 $^{+0.59}_{-0.45}$	–1.0(≥ -2.2)	0.55 $^{+0.48}_{-0.36}$	1(fixed)	0.19 $\times 10^{-13}$	1.27 $\times 10^{-13}$	28.1/25	NVSS J202723+405706
src4	2.2(≤ 6.7)	1.5 $^{+1.6}_{-1.3}$	–	–	0.06 $\times 10^{-13}$	1.47 $\times 10^{-13}$	16.0/25	TYC 3156-1302-1
src5	9 $^{+15}_{-7}$	1.6(≤ 4.1)	–	–	$\leq 0.01 \times 10^{-13}$	1.75 $\times 10^{-13}$	32.1/26	NVSS J202642+405138
src6	0(≤ 0.07)	1.72 $^{+0.47}_{-0.43}$	–	–	0.48 $\times 10^{-13}$	0.86 $\times 10^{-13}$	18.1/13	–
Source 2								
src1	2.33 $^{+0.86}_{-0.69}$	1.58 $^{+0.34}_{-0.30}$	–	–	0.24 $\times 10^{-13}$	5.46 $\times 10^{-13}$	120.8/101	–
src2	2.47(fixed ^b)	1.23 $^{+0.73}_{-0.83}$	–	–	0.02 $\times 10^{-13}$	0.92 $\times 10^{-13}$	20.3/24	–
src3	0.36 $^{+0.42}_{-0.30}$	1.92 $^{+0.49}_{-0.41}$	–	–	0.32 $\times 10^{-13}$	0.91 $\times 10^{-13}$	81.7/58	–
Background 1								
src1	2.5 $^{+1.7}_{-1.3}$	2.6 $^{+1.0}_{-0.9}$	–	–	0.34 $\times 10^{-13}$	3.00 $\times 10^{-13}$	18.0/19	several ^c
src2	3.1 $^{+8.8}_{-1.8}$	–	0.05 $^{+2.05}_{-0.02}$	1(fixed)	0.47 $\times 10^{-13}$	$\leq 0.01 \times 10^{-13}$	1.1/1	–
Background 2								
src1	0(≤ 18)	1.0(≤ 5.4)	–	–	0.15 $\times 10^{-13}$	0.79 $\times 10^{-13}$	15.0/17	NVSS J202754+423205
src2	1.5 $^{+3.7}_{-1.3}$	–	0.17 $^{+0.89}_{-0.14}$	1(fixed)	0.13 $\times 10^{-13}$	$\leq 0.01 \times 10^{-13}$	17.5/23	TYC 3160-1261-1

Γ is the photon index of the power-law model and kT and A are the temperature and abundance, respectively, in the plasma model. Abundance was fixed at the solar value if the value is not well constrained by a fit. $f_{0.5-2}$ and f_{2-10} are absorption-uncorrected fluxes in 0.5–2 keV and 2–10 keV, respectively.

^aObjects named NVSS and TYC are radio sources (Condon et al. 1998) and stars (Hog et al. 1998), respectively. IRXS denotes a source detected in the ROSAT All-sky survey (Voges et al. 1999).

^b $N(\text{H})$ is not well determined and is fixed to the estimated Galactic absorption.

^cCrowded region with several possible counterparts (stars, radio sources and H II regions.)

4. Discussion

4.1. Constraint on X-Ray Emission from the Cocoon

As shown in Table 2 and Figure 4, no significant excess has been found in the X-ray spectra of the extended emission in any of the four regions. However, the data have been fitted with the CXB+GRXE (plus local diffuse X-ray emission) model described in § 3.2 and the fitted GRXE component may include part of the cocoon emission, if any. To search for an excess above the expected GRXE profile, we have examined the positional dependence of the CXB-subtracted intensity. We have focused on the hard-band (2–10 keV), in which the relative contribution of an extended X-ray emission from the cocoon is expected to be highest.

Figure 5 shows how the intensity varies with Galactic latitude. The intensity of the CXB contribution is somewhat uncertain, due to uncertainty in the absorption and the field-to-field fluctuations of the CXB. To gauge the uncertainty of the absorption, we repeated the calculation of $N(\text{H})$ with spin temperature of 100 K and optical-thin approximation, and found the impact on 2–10 keV intensity is $\leq 0.46 \times 10^{-8} \text{ erg s}^{-1} \text{ cm}^{-2} \text{ sr}^{-1}$. According to Kushino et al. (2002), the field-to-field fluctuation of the CXB in the *ASCA*-GIS field-of-view ($\sim 0.4 \text{ deg}^2$) is 5.1% (1σ). Assuming that the fluctuation is Poisson’s noise, the expected fluctuation over the entire XIS field-of-view ($\sim 17'8 \times 17'8$) is $5.1 \times \sqrt{0.4/0.088} = 11\%$. Therefore the uncertainty of the CXB contribution in the 2–10 keV range is $(0.52\text{--}0.54) \times 10^{-8} \text{ erg s}^{-1} \text{ cm}^{-2} \text{ sr}^{-1}$. Uncertainty in the NXB model also affects the intensity of the extended emission. Tawa et al. (2008) reported that the reproducibility of the XIS NXB model (1σ) is $\sim 5\%$ and 3–4% in 1–7 keV and 5–12 keV ranges, respectively. We raised and lowered the NXB model by 5%, and found that the NXB-subtracted intensity in 2–10 keV was altered by $(0.26\text{--}0.63) \times 10^{-8} \text{ erg s}^{-1} \text{ cm}^{-2} \text{ sr}^{-1}$. We added the uncertainties due to the fluctuation of the CXB intensity and the NXB model reproducibility in quadrature, and took the effect from the assumption of spin temperature as systematic uncertainty. Even allowing for these uncertainties, the intensity profile (Figure 5) shows a clear monotonic decrease with increasing latitude, as expected for the GRXE. We have therefore concluded that most of the extended emission in the CXB-subtracted spectra in 2–10 keV is contributed by GRXE.

We therefore impose constraints on the extended X-ray emission from the cocoon. Among the four positions, the Galactic latitude is the highest in Background 2. Therefore, we expect the GRXE intensity to be minimized there and take the intensity of Background 2 as the lower limit of the GRXE contribution in the source positions. A robust upper limit on the extended X-ray emission from the cocoon can be obtained by subtracting the intensity in Background 2. In this way, the upper limit in the 2–10 keV range for Source 1 and Source 2 was determined as $3.4 \times 10^{-8} \text{ erg s}^{-1} \text{ cm}^{-2} \text{ sr}^{-1}$ and $1.3 \times 10^{-8} \text{ erg s}^{-1} \text{ cm}^{-2} \text{ sr}^{-1}$, respectively.

We have also calculated the expected synchrotron X-ray intensity from a CR electron spectrum which can reproduce the GeV emission of the cocoon by up scattering the interstellar and stellar radiation fields modelled in the region (Ackermann et al. 2011). The latter include the bright stars

of the Cyg OB2 and NGC 6910 associations, an average spectrum for the field stars, the intense IR field from the heated dust in the region, and the cosmological microwave background. The electron spectrum is based on the LIS one, which cuts off near 1 TeV, with power-law extensions up to 5, 10, 50, or 100 TeV. These spectra being too soft, we have applied an amplification factor of $120 \times (E/50 \text{ GeV})^{0.5}$ to account for the *Fermi*-LAT data. It yields an electron density of $2.6 \times 10^{-9} \text{ m}^{-3} \text{ TeV}^{-1}$ at 1 TeV. We have assumed a thickness of 25 pc for the emission region along the line-of-sight (corresponding to 1° at $d = 1.4 \text{ kpc}$ in the plane of the sky), and a magnetic field strength of $20 \mu\text{G}$ (deduced from pressure balance between the magnetic field and the gas)⁶. The synchrotron intensity expected in the 2–10 keV range from the electron spectrum extended to 100 TeV is $\sim 7.0 \times 10^{-8} \text{ erg s}^{-1} \text{ cm}^{-2} \text{ sr}^{-1}$. As the upper limits from the *Suzaku*-XIS observations are 1/5–1/2 of this value, we infer that our data are inconsistent with a pure inverse-Compton scenario in γ rays without a cut off in the electron spectrum.

To further constrain the CR properties, we have investigated the multi-wavelength spectra, including radio and TeV γ -rays as summarized in Figure 6. To compensate for the small field-of-view of the X-ray data compared to the size of the cocoon, we have integrated the averaged X-ray upper-limit (2–10 keV intensity of $2.35 \times 10^{-8} \text{ erg s}^{-1} \text{ cm}^{-2} \text{ sr}^{-1}$, or $9.13 \times 10^{-3} \text{ MeV}^2 \text{ s}^{-1} \text{ cm}^{-2} \text{ sr}^{-1} \text{ MeV}^{-1}$ assuming a photon index of 2.0) over the solid angle subtended by the cocoon ($4.38 \times 10^{-3} \text{ sr}$; Ackermann et al. 2011). A potential TeV counterpart to the cocoon, MGRO J2031+41, has been found by MILAGRO (Abdo et al. 2007, 2012). More recent results from the ARGO-YBJ experiment (Bartoli et al. 2014) confirm the presence of an extended TeV source of compatible position and size, even after subtracting the contribution from the known overlapping/nearby TeV sources. Its spectrum smoothly connects to the *Fermi*-LAT data points as described by Bartoli et al. (2014) (see also Fig. 6)⁷. The radio flux has been averaged over the cocoon from the CGPS survey (Taylor et al. 2003). The values should be considered as upper limits to the possible synchrotron emission from the cocoon because free-free emission from the hot ionized gas of Cygnus X has not been removed. The WMAP free-free map is too coarse and $H\alpha$ intensities are too absorbed in this region to allow a reliable subtraction of the free-free emission. The plotted curves for the synchrotron and inverse Compton models assume the amplified CR electron spectra described above, with the LIS cutting off near 1 TeV, and with power-law extensions to 5 TeV, 10 TeV, 50 TeV, and 100 TeV cut-offs. Our X-ray data require a cut-off in electron energy below 50 TeV, in agreement with the marked decline in TeV emission seen above 2 TeV (Abdo et al. 2012; Bartoli et al. 2014). The X-ray data should therefore be regarded as an independent confirmation of the spectral cutoff in the electron scenario inferred from TeV observations.

⁶ Although this value is larger than the local interstellar magnetic field strength, we have adopted it as Ackermann et al. (2011) examined possible solutions to explain the GeV/TeV γ -ray data while not violating the radio data in the specific environment of the cocoon.

⁷ Although VERITAS has surveyed the cocoon region, it was not able to detect the γ -ray emission on the angular scale of the Cygnus cocoon and MGRO J2031+41 with a standard ring-background estimation method, as described by Aliu et al. (2013).

4.2. Properties of GRXE and Local Diffuse X-rays

Finally we comment on the properties of GRXE and local diffuse X-ray emission. All four observations exhibit emission lines in the 0.5–0.6 keV range (see Figure 4). As shown in Table 2, the line central energy is ~ 0.55 keV and is not compatible with the O VII resonance line energy (0.574 keV) expected for the local hot plasma, but it is marginally consistent with the O VII forbidden line energy (0.561 keV) which is a signature of a charge-exchange process (e.g., Ebisawa et al. 2008; Fujimoto et al. 2007). We therefore conclude that SWCX significantly contributes to our data below 1 keV.

The intensity of the mid-temperature component (I_{mid} in Table 2) shows a positive correlation with Galactic latitude. This unusual behavior for GRXE may be attributed to the structure of the Cygnus Super Bubble (CSB). As shown by Uyaniker et al. (2001), the positions of the Source 2 and Background 2 images are inside or very close to the rim of the CSB, as seen by ROSAT in the 0.75 and 1.5 keV bands. Hence the intensity of the mid-temperature component should be significantly increased. We note that the $N(\text{H})_{\text{mid}}$ and kT_{mid} values of Source 2 and Background 2 are not compatible with the $N(\text{H}) \sim 0.3 \times 10^{22} \text{ cm}^{-2}$ and $kT \sim 0.3$ keV values ubiquitously found in CSB by Kimura et al. (2013). In particular, the Background 2 spectrum shows strong 0.7–1 keV emission (Fe-L and Ne lines), but lacks the line of O VIII, and therefore is not compatible with plasma emission at ~ 0.3 keV. Although *Suzaku* provides high-quality spectra compared to those in Kimura et al. (2013) in terms of energy range and resolution, our data correspond to a much smaller region, so a detailed discussion of the origin of this discrepancy is difficult and beyond the scope of this study.

The latitude dependence of the high-temperature component (I_{high} in Table 2) gives a scale height of $\sim 1.5^\circ$, which is 2–3 times larger than the GRXE scale height in the Scutum arm region close to the Galactic plane ($\sim 0.5^\circ$; e.g., Kaneda et al. 1997). This difference may be attributed to the proximity of Cygnus X (distance ~ 1.4 kpc), or to the different Galactic latitude ranges of the two studies ($b = 0.7\text{--}2.2$ deg in our observations whereas Kaneda et al. (1997) analyzed data in $b = 0\text{--}1.7$ deg). The observed temperature (2–3 keV) is significantly lower than the value of hard-temperature component of the GRXE reported for lower Galactic longitudes; e.g., kT of ~ 10 keV and ~ 5 keV were reported at $l \sim 28^\circ$ (Kaneda et al. 1997) and $l \sim 18^\circ$ (Uchiyama et al. 2009b), respectively. These Galactic longitude dependence of the temperature may provide useful information on the origin of GRXE (e.g., different populations of sources if GXRE is due to unresolved sources), but we defer a detailed discussion on this topic.

5. Summary

We have conducted a series of deep X-ray observations of the nearby star-forming region of Cygnus X using *Suzaku* XIS, in order to better understand the origin of the GeV emission revealed by *Fermi*-LAT in the cocoon of young cosmic rays pervading Cygnus X. After excluding

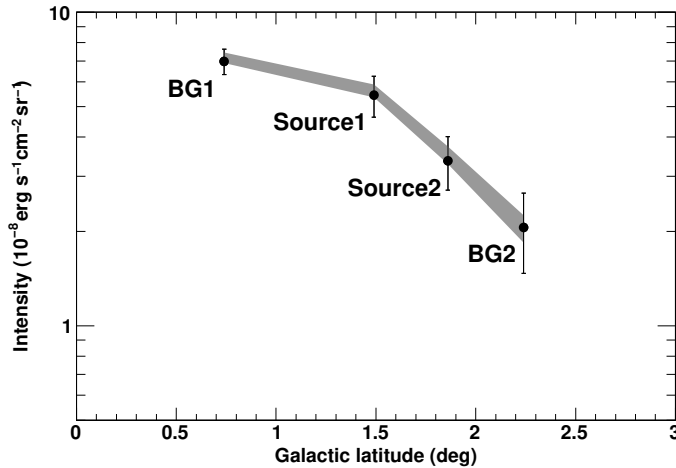


Fig. 5.— Dependence of the hard-band intensity (2–10 keV) on the Galactic latitude after subtracting the CXB contribution. The field-to-field fluctuation of the CXB intensity and the NXB model reproducibility are indicated by error bars, and the systematic uncertainty due to the absorption of the CXB model is shown by a shaded area.

point sources and small-scale structures from the X-ray images, and after subtracting the CXB, we find that the X-ray distribution in 2–10 keV band monotonically decreases with increasing Galactic latitude, thus indicating that most of the extended emission relates to the GRXE. We have obtained robust upper limits to the diffuse X-ray emission from the γ -ray cocoon. The results are incompatible with a pure inverse-Compton scenario for the origin of the γ -ray emission without a cut-off in the electron spectrum above about 50 TeV, in agreement with the drop observed in the γ -ray spectrum above 2 TeV. We have found a strong contribution of SWCX below 1 keV in our data. The mid-temperature component ($kT = 0.6$ – 0.7 keV) is likely to be significantly affected by the rim of CSB. The scale-height of the high-temperature component intensity (~ 1.5) is 2–3 times larger than the scale height of GRXE in the Scutum arm region at $l \sim 28^\circ$. We attribute this increased scale height to the proximity of Cygnus X. The observed temperature of the high-temperature component is 2–3 keV and is lower than found for the GRXE at smaller Galactic longitudes.

We would like to thank K. Ebisawa, K. Hayashida and S. Yamauchi for valuable comments. We also thank the Suzaku team members for their dedicated support of the satellite operation and calibration.

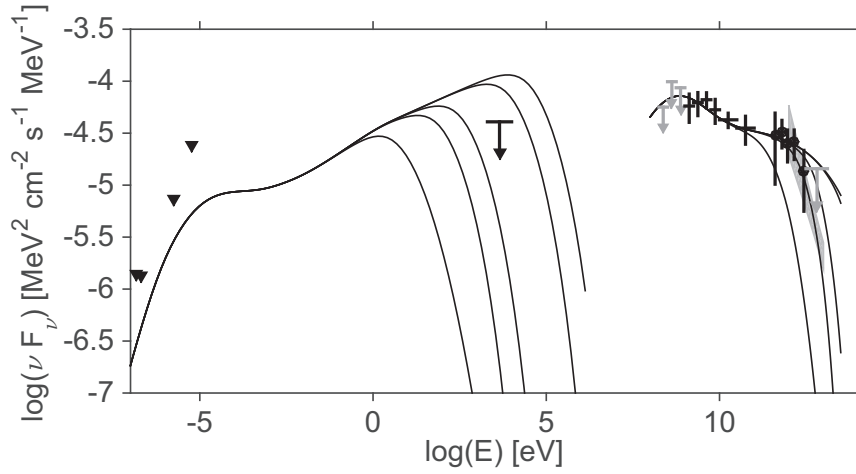


Fig. 6.— Multi-wavelength data and models of the emission from the Cygnus cocoon region: the data points in the 0.1–100 GeV band come from the *Fermi*-LAT data (Ackermann et al. 2011), the data points and the power-law model at TeV energies from the ARGO-YBJ (Bartoli et al. 2014) and the MILAGRO (Abdo et al. 2012) experiments, respectively, the X-ray upper limit from the present work, and the radio upper limits (triangles) from the CGPS survey (Taylor et al. 2003). At TeV energies the MILAGRO data likely include all sources around the cocoon area, but below 10 TeV the flux exceeds the sum from TeV J2032+4130 (Aharonian et al. 2005) and VER J2019+407 (Aliu et al. 2013) by at least a factor of two. Thin lines show the modelled synchrotron and inverse Compton emissions, assuming an amplified LIS electron spectrum, or this spectrum with power-law extensions to cut-off energies of 5, 10, 50, and 100 TeV. See text for details.

REFERENCES

- Abdo, A. A., Allen, B., Berley, D., et al. 2007, ApJ, 664, 91
- Abdo, A. A., Abeysekara, A. U., Allen, B. T., et al. 2012, ApJ, 753, 159
- Ackermann, M., Ajello, M., Allafort, A., et al. 2011, Science, 334, 1103
- Ackermann, M., Ajello, M., Atwood, W. B., et al. 2012a, ApJ, 750, 3
- Ackermann, M., Ajello, M., Allafort, A., et al. 2012b, A&A, 538, 71
- Atwood, W. B., Abdo, A. A., Ackermann, M., et al. 2009, ApJ, 697, 1071
- Aharonian, F., Akhperjanian, A., Beilicke, M., et al. 2005, A&A, 431,197
- Aliu, E., Archambault, S., Arlen, T., et al. 2013, ApJ, 770, 93
- Bartoli, B., Bernardini, P., Bi, X. J., et al. 2014, ApJ, 790, 152
- Bykov, A. M., & Fleishman, G. D. 1992, MNRAS, 255, 269
- Condon, J. J., Cotton, W. D., Greisen, E. W., et al. 1998, AJ, 115, 1693
- Ebisawa, K., Tsujimoto, M., Paizis, A., et al. 2005, ApJ, 635, 214
- Ebisawa, K., Yamauchi, S., Tanaka, Y., et al. 2008, PASJ, 60, S223
- Fujimoto, R., Mitsuda, K., Mccammon, D., et al. 2007, PASJ, 59, 133
- Ginzburg V.I., & Syrovatskii S.I. 1964, *the Origin of Cosmic Rays*, Pergamon Press. Classic monograph
- Grenier, I. A., Casandjian, J.-M., Terrier, R. 2005, Science 307, 1292
- Higdon, J. C., & Lingenfelter, R. E. 2005, ApJ, 628, 738
- Hog, E., Kuzmin, A., Bastian, U., et al., 1998, A&A, 335, 65
- Ishisaki, Y., Maeda, Y., Fujimoto, R., et al. 2007, PASJ, 59, S113
- Kalberla, P. M. W., Burton, W. B., Hartmann, D., et al. 2005, A&A, 440, 775
- Kaneda, H., Makishima, K., Yamauchi, S., et al. 1997, ApJ, 491, 638
- Kataoka, J., Tahara, M., Totani, T., et al. 2013, ApJ 779, 57
- Kimura, M., Tsunemi, H., Tomida, H., et al. 2013, PASJ, 65, 14
- Koyama, K., Makishima, K., Tanaka, Y., & Tsunemi, H. 1986, PASJ, 38, 121

- Koyama, K., Tsunemi, H., Dotani, T., et al. 2007, PASJ, 59, S23
- Kushino, A., Ishisaki, Y., Morita, U., et al. 2002, PASJ, 54, 327
- Mitsuda, K., Bautz, M., Inoue, H., et al. 2007, PASJ, 59, S1
- Morisson, R., & McCammon, D. ApJ, 270, 119
- Parizot, E., Marcowith, A., van der Swaluw, E., et al. 2004, A&A, 424, 747
- Piddington, J. H., & Minnett, H. C. 1952, Australian J. Sci. Res., 5, 17
- Revnivtsev, M., Sazonov S., Gilfanov, M., Churazov, E., & Sunyaev, E. 2006, A&A, 452, 169
- Rygl, K. L. J., Brunthaler, A., Sanna, A., et al. 2012, A&A, 539, 79
- Serlemitsos, P. J., Soong, Y., Chan, K.-W., et al. 2007, PASJ, 59, 59
- Smith, R. K., Bautz, M. W., Edgar, R. J., et al. 2007, PASJ 59, S141
- Smith, R. K., Brickhouse, N. S., Liedahl, D. A., & Raymond, J. C. 2001, ApJ, 556, 91
- Tawa, N., Hayashida, K., Nagami, M., et al. 2008, PASJ, 60, 11
- Taylor, A. R., Gibson, S. J., Peracaula, M., et al. 2003, AJ, 125, 3145
- Tenorio-Tagle, G., & Bodenheimer, P. 1988, ARA&A, 26, 145
- Tozzi, P., Rosati, P., Nonino, M., et al. 2001, ApJ, 562, 42
- Uchiyama, H., Ozawa, M., Matsumoto, H. et al. 2009a, PASJ, 61, S9
- Uchiyama, H., Matsumoto, H., Tsuru, T. G., Koyama, K., & Bamba, A. 2009b, PASJ, 61, S189
- Uchiyama, H., Nobukawa, M., Tsuru, T. G., & Koyama, K. 2013, PASJ, 65, 19
- Uyaniker, H., Fürst, E., Reich, W., Aschenbach, B., & Wielebinski, R. 2001, A&A, 371, 675
- Voges, W., Aschenbach, B., Boller, T., et al. 1999, A&A, 349, 389
- Warwick, R. S., Turner, M. J. L., Watson, M. G., & Willingale, R. 1985, Nature, 317, 218
- Worrall, D. M., Marshall, F. E., Boldt, E. A., & Swank, J., M. 1982, ApJ, 255, 111
- Yoshino, T., Mitsuda, K., Yamasaki, N. Y., et al. 2009, PASJ, 61, 805